PHYSICAL REVIEW MATERIALS **6**, 084410 (2022)

Ce and Dy substitutions in $Nd_2Fe_{14}B$: Site-specific magnetic anisotropy from first principles

James Boust,[1] Alex Aubert,[2] Bahar Fayyazi,[2] Konstantin P. Skokov,[2] Yurii Skourski,[3]
Oliver Gutfleisch,[2] and Leonid V. Pourovskii[1,4]
[1]*CPHT, Ecole Polytechnique, CNRS, Institut polytechnique de Paris, 91128 Palaiseau, France*
[2]*Functional Materials, TU Darmstadt, 64287 Darmstadt, Germany*
[3]*Dresden High Magnetic Field Laboratory (HLD-EMFL), Helmholtz-Zentrum Dresden Rossendorf, D-01328 Dresden, Germany*
[4]*Collège de France, 11 Place Marcelin Berthelot, 75005 Paris, France*

(Received 2 May 2022; accepted 30 June 2022; published 29 August 2022)

A first-principles approach combining density-functional and dynamical mean-field theories in conjunction with a quasiatomic approximation for the strongly localized $4f$ shell is applied to $Nd_2Fe_{14}B$-based hard magnets to evaluate crystal-field and exchange-field parameters at rare-earth sites and their corresponding single-ion contribution to the magnetic anisotropy. In pure $Nd_2Fe_{14}B$, our calculations reproduce the easy-cone to easy-axis transition; theoretical magnetization curves agree quantitatively with experiment. Our study reveals that the rare-earth single-ion anisotropy in the 2-14-1 structure is strongly site dependent, with the g rare-earth site exhibiting a larger value. In particular, we predict that increased f- and g-site occupancy of $R =$ Ce and Dy, respectively, leads to an increase of the magnetic anisotropy of the corresponding $(\mathrm{Nd}, R)_2\mathrm{Fe}_{14}\mathrm{B}$-substituted compounds.

DOI: 10.1103/PhysRevMaterials.6.084410

I. INTRODUCTION

High-performance permanent magnets are key components of numerous energy-efficient technologies which have today met an increasing need, such as wind generators and electrical motors [1–4]. Understanding and optimizing their intrinsic properties arising at the atomic level as well as their extrinsic properties due to the microstructure is therefore crucial economically and environmentally wise [1]. The market is dominated by rare-earth (R) transition-metal (M) intermetallics [1,5] whose intrinsic properties are generally understood within the two sublattice picture [6]: the itinerant $3d$ electrons of a late transition metal, such as Fe and Co, provide the compound with strong permanent magnetism behavior (i.e., large magnetization and Curie temperature) while the magnetic hardness mainly stems from the R-localized $4f$ shells, whose strong spin-orbit coupling converts the crystal-field anisotropy into a magnetic one. The interplay between these two sublattices is governed by the M-induced exchange field, the $4f - 4f$ interaction usually being much weaker [7–9] and neglected.

The most widely used high-performance permanent magnet in the industry is the $Nd_2Fe_{14}B$ (2-14-1) intermetallic, in which Nd is often partially substituted by heavy R's such as Dy or Tb to further enhance the magnetic properties [1,3–5]. However, substantial efforts are being made to find alternative hard magnets with reduced critical R content because of their economical as well as environmental costs [2–4]. For instance, there is growing interest in Ce, which is far more abundant than Nd [4,10,11].

Within this context, understanding the intrinsic properties of complex 2-14-1 systems with partial Nd substitution would help in optimizing the design of new hard magnets. It requires, however, a quantitative description of crystal-field effects, which induce the single-site rare-earth magnetic anisotropy and, thus, the magnetic hardness in these systems. A reliable evaluation of crystal field parameters (CFPs) is a difficult task both from experimental and theoretical perspectives. Indeed, extracting them by fitting experimental high-field magnetization curves [12–14] has a limited predictive power, as it usually neglects some CFPs and requires the use of single crystals. Furthermore, care must be taken to properly separate contributions from the M and R sublattices [15]. An alternative route is to compute these CFPs from first principles, which is also a notorious challenge, notably due to the localized and strongly correlated nature of R $4f$ states which standard density functional theory (DFT) fails to describe properly. $Nd_2Fe_{14}B$-based systems are especially hard to treat due to a large unit cell with two inequivalent R sites. Early works toward *ab initio* methods were still partially relying on the crude point-charge electric model [16,17]. Several DFT-based approaches have so far been developed and applied to various R-M intermetallics [18–22], but they usually rely on open-core-like treatment of R $4f$ shells, neglecting R-M hybridization. The latter can have a significant impact on CFPs and magnetic properties [23]. Regarding 2-14-1 systems, after early studies focusing on the '20' CFP [24,25], authors of Refs. [26–29] used a Wannier-function-based approach to compute all CFPs in various compounds but hybridization was taken into account in an approximate way [26].

Recently, Delange *et al.* [30] introduced an approach to the first-principles calculation of CFPs in such intermetallics by treating the $4f$ shell, in the framework of the dynamical mean-field theory (DMFT) [31,32], within the quasiatomic Hubbard-I (HI) approximation [33]. This DFT+DMFT [34] method removes the unphysical $4f$ self-interaction contribution to the CF by an averaging scheme. It was successfully applied to $R\mathrm{Co}_5$ compounds by Pourovskii *et al.* [23] who explained the 40-year-old mystery of the measured zero-temperature Nd magnetic moment in NdCo_5 [35] being frozen below saturation by a large high-rank ‘66’ CFP arising from the hybridization with neighboring Co atoms. Hybridization can be implicitly taken into account in this methodology by a proper choice of the $4f$ Wannier projection window.

Building on this success, we apply in this paper the same methodology to 2-14-1 systems. Comparison of our computed CFPs and resulting magnetic properties with experimental data shows that this essentially *ab initio* approach can accurately capture intrinsic magnetic properties of the parent $\mathrm{Nd_2Fe_{14}B}$ compound such as the temperature evolution of the spontaneous magnetization direction and magnetization curves. We then focus on site-specific partial Nd substitutions by either Dy or Ce. Our main results are (i) the CFPs on a given inequivalent R site are not sensitive to substitutions on the second R site and (ii) the R single-ion anisotropy (SIA) is strongly site dependent. We therefore predict that optimization of site occupancy in Ce- and Dy-substituted $\mathrm{Nd_2Fe_{14}B}$ could lead to an increase, though moderate, of magnetic anisotropy. We also measure the impact of Ce substitution on magnetocrystalline anistropy energy (MAE) in single crystals and compare it with theoretical predictions.

The paper is organized as follows: In Sec. II, we review the theoretical methodology and experimental procedures used in this work; in Sec. III, we present our results on pure $\mathrm{Nd_2Fe_{14}B}$ as well as Ce- and Dy-substituted compounds.

II. THEORETICAL APPROACH

A. Electronic structure calculations

The electronic-structure calculations of rare-earth transition-metal intermetallics are carried out using the DFT+HI approach of Refs. [23,30]. Within this self-consistent over the charge density DFT+DMFT scheme [34], the local-spin density approximation (LSDA) is employed to describe the M magnetism while the quasiatomic HI [33] approximation for the DMFT [31,32] impurity problem is used to describe the $R\,4f$ shell. La is treated within LSDA as its $4f$ shell is empty (La^{3+}). Spin-orbit coupling is included within the standard second-variation procedure as implemented in Ref. [36]. The experimental crystal structure (space group $P4_2/mnm$) and lattice parameters are used [37] throughout; lattice distortions with temperature [38] are neglected. To evaluate the lattice parameters of the mixed $(RR')_2\mathrm{Fe_{14}B}$ systems from those of the corresponding pure compounds, we employ Vegard’s law. Calculations are performed with the M magnetic moment aligned along the [001] direction. The approach is implemented within the full-potential linearized augmented plane wave band structure code WIEN2K [36,39] in conjunction with the TRIQS library [40,41].

$R\,4f$ Wannier orbitals are constructed from the Kohn-Sham (KS) bands enclosed in an energy window of size 4 eV. As in Ref. [23], for Nd, whose KS $4f$ states are pinned at the Fermi level E_F, this window is centered around E_F; for Dy, as the $4f$ KS bands move toward lower energies during the self-consistent calculation, the window is centered around the central weight of the $4f$ partial density of states. This window should be large enough to enclose most of the $4f$ KS states but small enough to capture the hybridization with M atoms which, as shown in Ref. [23], is crucial to the proper evaluation of CFPs.

Within the HI approximation, the DMFT impurity problem is reduced [42] to the diagonalization of the following quasiatomic Hamiltonian for the $4f$ shell:

$$\hat{H}_{\mathrm{at}} = \hat{H}_{1\mathrm{el}} + \hat{H}_U = \sum_{mm'\sigma\sigma'} \epsilon_{mm'}^{\sigma\sigma'} \hat{f}^{\dagger}_{m\sigma} \hat{f}_{m'\sigma'} + \hat{H}_U. \tag{1}$$

Here, $\hat{f}_{m'\sigma'}$ is the annihilation operator for the $4f$ orbital $m'\sigma'$, $\hat{H}_U$ is the Coulomb repulsion Hamiltonian, and $\epsilon_{mm'}^{\sigma\sigma'}$ is the one-electron level-position matrix:

$$\epsilon = -(\mu + \Sigma_{\mathrm{DC}})\mathbb{I} + \sum_{\mathbf{k}\in\mathrm{BZ}} P_{\mathbf{k}} H_{\mathrm{KS}}^{\mathbf{k}} P_{\mathbf{k}}^{\dagger}, \tag{2}$$

where $\mathbb{I}$ is the identity matrix, μ is the chemical potential, Σ_{DC} is the double-counting correction computed here within the fully localized limit (FLL) with nominal atomic occupancy [43], $H_{\mathrm{KS}}^{\mathbf{k}}$ is the KS Hamiltonian matrix, and $P_{\mathbf{k}}$ is the projection matrix between the $4f$ Wannier and KS spaces [34].

The Coulomb interaction $\hat{H}_U$ is specified by the parameters $J_H = 0.77$ (0.99) eV (as measured by optical spectroscopy [44]) and $U = 6$ (7) eV for Nd (Dy), respectively.

B. Single-ion model for the $4f$ Hamiltonian

Once the DFT+HI scheme described in the previous subsection has converged, the CFPs, spin-orbit coupling, and exchange field are extracted by fitting the converged one-electron part $\hat{H}_{1\mathrm{el}}$ of the quasiatomic Hamiltonian Eq. (1) onto the form expected within the single-ion model (which neglects $4f-4f$ interactions), namely, for a R ion embedded in a 2-14-1 crystal with ferromagnetically aligned M moments, it reads

$$\hat{H}_{1\mathrm{el}} = E_0\hat{\mathbb{I}} + \lambda\sum_i \hat{s}_i\hat{l}_i + \hat{H}_{\mathrm{ex}} + \hat{H}_{\mathrm{CF}} + \hat{H}_{\mathrm{ext}}. \tag{3}$$

E_0 is an energy shift, λ is the spin-orbit coupling, $\hat{H}_{\mathrm{ex}} = 2\mu_B\mathbf{B}_{\mathrm{ex}}(T)\cdot\hat{\mathbf{S}}_{4f}$ is the M-R exchange interaction with $\mathbf{B}_{\mathrm{ex}}(T)$ being the exchange field at temperature T, and $\hat{\mathbf{S}}_{4f}$ the $4f$ spin operator. The M-R exchange interaction is a multiorbital coupling as it has been shown to be mediated by the moment of $R5d6s$ orbitals [37,45]. The exchange field $\mathbf{B}_{\mathrm{ex}}(T)$ used in the single-ion model captures the combined effects of the interatomic $M3d-R5d6s$ and intra-atomic $R5d6s-R4f$ [46,47] interactions as an effective mean-field acting on the $R4f$ shell.

$\hat{H}_{\mathrm{CF}}$ is the crystal-field Hamiltonian, which, in 2-14-1 compounds, in the coordinate system x $\|$[100] and z $\|$[001], can be written as [12]

$$\begin{aligned}\hat{H}_{\mathrm{CF}} = {} & L_2^0\hat{T}_2^0 + L_2^{-2}\hat{T}_2^{-2}\\ & + L_4^0\hat{T}_4^0 + L_4^{-2}\hat{T}_4^{-2} + L_4^4\hat{T}_4^4\\ & + L_6^0\hat{T}_6^0 + L_6^{-2}\hat{T}_6^{-2} + L_6^4\hat{T}_6^4 + L_6^{-6}\hat{T}_6^{-6},\end{aligned}$$

where $\hat{T}_k^q$ are the Hermitian combination of Wybourne’s operators [48] with the same notations as Ref. [30] and L_k^q are the CFPs. As often done in the literature, we will use the Stevens

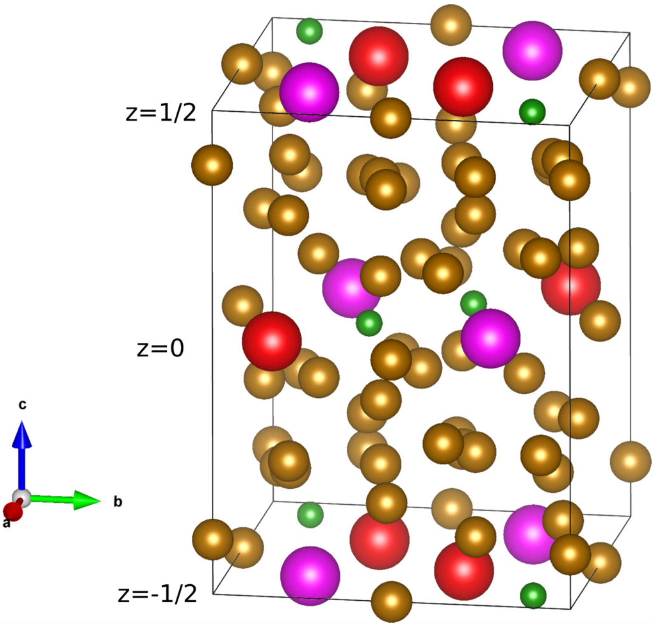

FIG. 1. 2-14-1 crystal structure showing the different z planes and inequivalent R sites discussed in the main text: R f site in purple, R g site in red (Fe: large brown, B: small green). These sites are also often labeled as $4f$ and $4g$ in the literature but we keep f and g in this paper to avoid confusion with the notation for the R $4f$ electrons. Plotted with VESTA [51].

convention [49] of the CFPs throughout, $A_k^q\langle r^k\rangle = \lambda_{kq}L_k^q$ (λ_{kq} are tabulated in Ref. [50], for instance). We neglect possible temperature dependence of CFPs [13].

$\hat{H}_{\mathrm{ext}} = -\mathbf{H}_{\mathrm{ext}} \cdot \hat{\mathbf{M}}_{4f}$ is the Zeeman interaction between the total $4f$ moment operator $\hat{\mathbf{M}}_{4f}$ and the external magnetic field $\mathbf{H}_{\mathrm{ext}}$.

With the M sublattice magnetism treated by zero-temperature LSDA, the term $\hat{H}_{\mathrm{ex}}$ is obtained for $T = 0$ (and the external field $\mathbf{H}_{\mathrm{ext}}$ is zero). The CFPs, spin-orbit coupling, and exchange field are extracted this way for the two inequivalent R sites, labeled f and g, as well as for the two $z = 0$ and $z = 1/2$ planes [37] (cf. Fig. 1, plotted with VESTA [51]). To remove the unphysical $4f$ contribution to the CF splitting and exchange field, the DFT+HI scheme described above also employs a self-interaction correction; the computed CFPs are furthermore weakly dependent on the values of U and J_H [30].

C. Two sublattice model of $3d - 4f$ intermetallics

The results of the previous subsection [i.e., the one-electron $4f$ Hamiltonian defined in Eq. (3), with its parameters calculated *ab initio* for each R site in the unit cell] are then employed within the two-sublattice picture of rare-earth transition-metal intermetallics. The latter decomposes the total free energy F of a $(R_{1-x}R'_x)_2\mathrm{Fe}_{14}\mathrm{B}$ system as

$$F(T) = \sum_i w_i F_{4f}^{(i)}(T) + F_{3d}(T), \tag{4}$$

$$F_{3d}(T) = -\boldsymbol{M}_{3d}(T)\cdot\boldsymbol{H}_{\mathrm{ext}} + K_1^{3d}(T)\sin^2\theta_{3d}, \tag{5}$$

$$F_{4f}^{(i)}(T) = -T\log\left(\mathrm{Tr}\left[\exp\left\{-\beta\left(\hat{H}_{1\mathrm{el}}^{(i)} + \hat{H}_U\right)\right\}\right]\right), \tag{6}$$

where w_i is the occupancy of magnetic (Nd or Dy) ion $i =$ (R, site, plane), $K_1^{3d}(T)$ is the first anisotropy constant of the M sublattice, θ_{3d} is the angle between the M moment $\boldsymbol{M}_{3d}(T)$ and the [001] axis, $\beta = 1/(k_BT)$. The calculation of the $4f$ free energy Eq. (6) is performed by taking into account states of the groundstate and first excited multiplets – the importance of the latter has been pointed out in previous works [12,23]. Magnetization curves can then be obtained by minimizing Eq. (4) with respect to θ_{3d}. In the following Secs. II D and II E, we explain how we set the parameters describing the $3d$ sublattice in Eqs. (4)–(6), namely, $M_{3d}(T)$, $B_{\mathrm{ex}}(T)$, and $K_1^{3d}(T)$.

D. $3d$ sublattice at zero temperature

We assume the zero temperature K_1^{3d} to be independent on the R ions and evaluate it in $\mathrm{La}_2\mathrm{Fe}_{14}\mathrm{B}$ by performing two separate LSDA+U calculations with the M moment aligned along [001] and [100], with $U - J = 1.1$ eV for the M $3d$ shells. We then employ the method of Ref. [52] computing K_1^{3d} from the change of M sublattice spin-orbital energy upon its moment rotation,

$$K_1^{3d} = \sum_i \Delta E_i^{\mathrm{SO}}/2, \tag{7}$$

where the sum runs over all M ions, $\Delta E_i^{\mathrm{SO}} = E_i^{\mathrm{SO}}(\boldsymbol{M}_{3d}||100) - E_i^{\mathrm{SO}}(\boldsymbol{M}_{3d}||001)$. The spin-orbit energy E_i^{SO} for site i is calculated as $\mathrm{Tr}[\rho_i^{3d}\hat{H}_{\mathrm{SO}}^{3d}]$, where ρ_i^{3d} is the on-site $3d$ density matrix for a given $\boldsymbol{M}_{3d}$ direction and the spin-orbit Hamiltonian $\hat{H}_{\mathrm{SO}}^{3d}$ is of the same form as for the R shell but with the LSDA+U-estimated value $\lambda_{\mathrm{Fe}} = 60$ meV. This approach yields the value $K_1^{3d} = 0.4$ MJ.m^{-3} for $\mathrm{La}_2\mathrm{Fe}_{14}\mathrm{B}$, in reasonable agreement with experimentally measured value [53] $K_1^{3d} = 0.7$ MJ.m^{-3}.

At 0 K, both B_{ex} and the $3d$ spin moment are extracted from the material specific DFT+HI scheme described in Sec. II A, namely, B_{ex} is extracted from the converged one-electron $4f$ Hamiltonian as described in Sec. II B. The $3d$ spin moment S_{3d} is calculated simultaneously. Note that since the R spin-polarization is suppressed in the calculated DFT+HI charge density, as described in Ref. [30], the resulting DFT+HI total spin moment corresponds to S_{3d}. It is found to be essentially the same (30 μ_B/f.u.) in $\mathrm{Nd}_2\mathrm{Fe}_{14}\mathrm{B}$ and $\mathrm{Dy}_2\mathrm{Fe}_{14}\mathrm{B}$. Since B_{ex} originates from the same $3d$ spin polarization in the same calculation, this treatment ensures consistent values of these parameters.

We expect the $3d$ zero-temperature orbital moment L_{3d} to be essentially independent on the R ions in the system. We therefore add to S_{3d} the value of L_{3d} computed by LSDA+U in $\mathrm{La}_2\mathrm{Fe}_{14}\mathrm{B}$, yielding 0.06 μ_B/atom (in reasonable agreement with the experimental value of $\sim$0.08 μ_B/atom [54]) and a total moment per unit cell of $M_{3d} = L_{3d} + S_{3d} = 30.8$ μ_B at zero temperature.

E. Temperature scaling of the $3d$ sublattice

Consistent with the definition of the exchange field, $\mathbf{M}_{3d}(T)$ and $\mathbf{B}_{\mathrm{ex}}(T)$ are assumed to be antialigned (as is the case in our calculations for $T = 0$) and, neglecting the temperature variation of the exchange coupling constant, to follow

TABLE I. Values of the Curie temperature T_C (in K) and of the $3d$ first anisotropy constant at 0 K K_1^{3d} (in MJ.m^{-3}) involved in the two-sublattice model for different compounds.

	T_C	K_1^{3d}
$Nd_2Fe_{14}B$	585	0.4
$Ce_2Fe_{14}B$	424	1.6
$(Ce_{0.63}Nd_{0.37})_2Fe_{14}B$	484	1.16
$(Ce_{0.36}Nd_{0.64})_2Fe_{14}B$	527	0.83
$Dy_2Fe_{14}B$	598	0.4
$(Dy_{0.36}Nd_{0.64})_2Fe_{14}B$	590	0.4

the same temperature scaling, for which we use Kuz'min's semiempirical one [55]:

$$M_{3d}(T) = M_{3d}\alpha(T), \tag{8}$$

$$B_{\rm ex}(T) = B_{\rm ex}\alpha(T), \tag{9}$$

$$\alpha(T) = \left[1 - s\left(\frac{T}{T_C}\right)^{\frac{3}{2}} - (1-s)\left(\frac{T}{T_c}\right)^{p}\right]^{\frac{1}{3}}, \tag{10}$$

where T_C is the Curie temperature taken from experiment [37] for pure compounds and computed as the weighted sum of parent pure compounds for mixed systems (cf. Table I). We use $s = 0.6$ and $p = 5/2$ in accordance with Ref. [56].

$K_1^{3d}(T)$ is assumed to follow the temperature scaling of Zener [57] (although it is a rather simplistic approximation in 2-14-1 systems, as shown in Refs. [53,58,59]),

$$K_1^{3d}(T) = K_1^{3d}(M_{3d}(T)/M_{3d})^3,$$

which gives $K_1^{3d}(T) = K_1^{3d}\alpha(T)^3$.

F. Treatment of Ce-based compounds

A special treatment is necessary for Ce-based compounds which we explain here. Indeed, according to the measurements of Ref. [60], Ce is found in an intermediate valence state dominated by Ce^{4+} in 2-14-1 intermetallics, the description of which would require the use of more sophisticated and computationally heavy many-body approaches such as quantum Monte Carlo [61]. Moreover, in 2-14-1 systems with localized rare earth, those localized R ions (Nd, Dy, etc.) provide a dominant contribution to the magnetic anisotropy. The contribution of Ce, whether with an itinerant or localized $4f$ shell, is expected to be relatively small, in particular, at room temperature and above (as shown in Ref. [61]). Therefore, in mixed compounds $(Nd_{1-x}Ce_x)_2Fe_{14}B$:

(1) Ce is treated within LSDA for CFP calculations of Nd by the DFT+HI scheme described above.

(2) Ce contributions to the magnetic moment and anisotropy in the two-sublattice model are described by a mere renormalization of the same $3d$ quantities at zero temperature. Specifically, as the total experimental moment per unit cell in $Ce_2Fe_{14}B$ is 29.4 μ_B at 4.2 K [37], we adapt $M_{3d} = 30.8(1-x) + 29.4x$ μ_B per unit cell. Furthermore, as we measured a larger zero temperature $K_1 = 1.6$ MJ.m^{-3} in $Ce_2Fe_{14}B$ (in agreement with previous measurements [53,59]) compared to $La_2Fe_{14}B$, we adapt $K_1^{3d} = 0.4(1-x) + 1.6x$ MJ.m^{-3} (cf. Table I).

III. EXPERIMENTAL METHODS

$(Nd_{1-x}Ce_x)_2Fe_{14}B$ ($x = 0$, 0.63, 1) single crystals were grown using the reactive flux method as described in our previous study [62].

The chemical composition was determined using energy dispersive x-ray spectroscopy equipped in a Philips XL30 FEG scanning electron microscopy. The single crystallinity and crystallographic orientation of the single crystals were verified using a back-scattering Laue camera. The magnetization measurement was performed using a physical properties measurement system (PPMS 14, Quantum Design) with vibrating sample magnetometer up to 14 T at temperatures ranging from 10 to 300 K. For magnetization measurements at fields up to 50 T, a pulsed-field magnetometer built at the High-field Laboratory in Dresden-Rossendorf was used, as described in detail in Ref. [63]. The MAE was extracted from the experimental results by calculating the integral of the $M(H)$ curves for [100] and [001] axes (hard and easy axis at RT, respectively), and we subtracted the integral of the [001] (which is taken as reference, also below spin reorientation) from the one of [100].

IV. RESULTS

A. Crystal-field parameters and exchange field

Nd CFPs and $B_{\rm ex}$ computed within our approach (cf. Secs. II A and II B) in $Nd_2Fe_{14}B$, together with experimental [13,64] and previous *ab initio* [29] values, are summarized in Fig. 2 for f and g inequivalent sites in the unit cell. Our theoretical parameters have the same sign and order of magnitude as the ones extracted by Ref. [13] from experimental magnetization curves (only a subset of CFPs was assumed to be nonzero in their fitting). The only significant discrepancy with respect to Ref. [13] is the underestimation of $A_6^4\langle r^6\rangle$ on the g site. Overall, the results of our *ab initio* approach are comparable with those of Ref. [29].

The precise values are summarized in Table III in the Appendix, which also lists computed CFPs for Dy as well as our results for various mixed systems with Ce or La (both treated within LSDA) occupying one of the two sites. These calculations with partial substitution give, for Nd and Dy, essentially the same CFPs and $B_{\rm ex}$ as in the corresponding pure compounds. This shows that the CFPs on one R site are insensitive to substitution of the R element at the other site, therefore justifying the use of Eq. (4).

Furthermore, in all cases, the g site exhibits higher or equal $A_2^0\langle r^2\rangle$ and $B_{\rm ex}$ compared to the f site. This suggests that the g site exhibits a higher SIA than the f one (in agreement with the results of Refs. [10,29]), at least at high temperature, where higher order CFPs are essentially negligible. This idea will be explored in the last two subsections.

B. Magnetic properties of pure $Nd_2Fe_{14}B$

We employ the computed CFPs shown in Fig. 2 and parameters summarized in Table I within the two-sublattice picture (cf. Secs. II C–II E) to compute magnetic properties of $Nd_2Fe_{14}B$ and compare our predictions with experimental data.

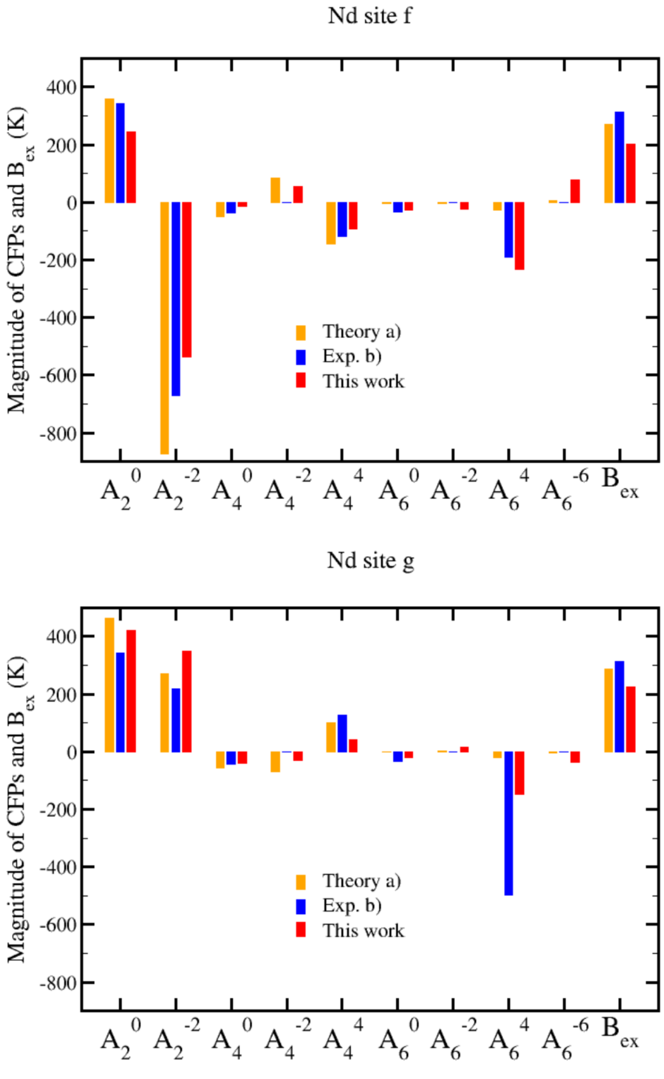

FIG. 2. Nd CFPs and B_{ex} (in K) for both inequivalent sites in the 2-14-1 system. The values are for the $z = 0$ plane of the unit cell (the signs of $A_2^{-2}\langle r^2\rangle$, $A_4^{-2}\langle r^4\rangle$, $A_6^{-2}\langle r^6\rangle$, and $A_6^{-6}\langle r^6\rangle$ change for the middle plane). (a) Ref. [29]. (b) Ref. [13] (Ref. [64] for B_{ex}).

Figure 3 displays the computed $Nd_2Fe_{14}B$ magnetization curves along the [100] and [110] directions together with the experimental ones [62] at $T = 10$ K and 300 K. The experimental curves are well reproduced, including some subtle features such as the first-order magnetization process (FOMP) along [100] at $T = 10$ K (at $H_{ext} = 17$ T) as well as the saturation ($\sim 37\ \mu_B$/f.u. along [100] at 10 K) and spontaneous magnetizations ($\sim 13\ \mu_B$/f.u. and $\sim 17\ \mu_B$/f.u. at 10 K along [100] and [110], respectively).

Figure 4 shows the evolution of the angle θ between the total spontaneous magnetization and the [001] axis (in the (110) plane) in $Nd_2Fe_{14}B$. Our calculations reproduce the spin reorientation transition (SRT) occurring at low temperature. The low-temperature angle is also reproduced ($\sim 30°$), which is consistent with the excellent agreement of the low-temperature magnetizations at zero field (Fig. 3). The SRT temperature is, however, underestimated (~ 75 K instead of 135 K). There has been a lot of debate regarding the magnetic structure of the compound at 4 K: some works [12,13,65] predicted a very small canting angle between Nd moments and the total one ($\leqslant 7°$), while others suggested a large one [66–69]. Our calculations support the small canting angle picture, with a maximum angle of 5° between a Nd moment and the total one.

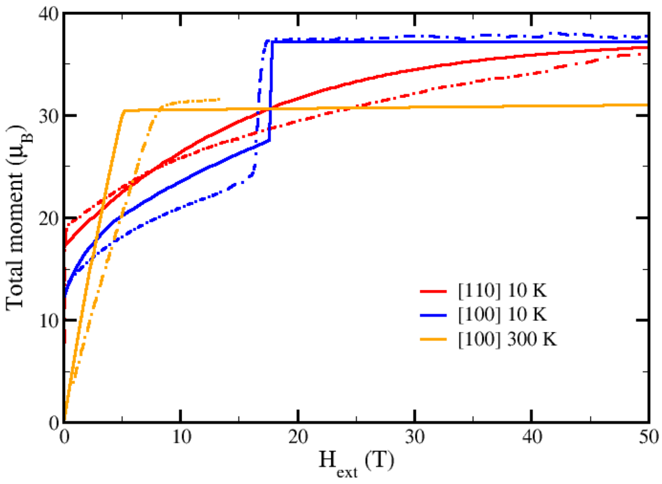

FIG. 3. $Nd_2Fe_{14}B$ magnetization curves (per f.u.), along [100] and [110], at $T = 10$ and 300 K. Dotted lines: experiment [62]. Solid lines: theory.

Figure 5 displays the evolution of $Nd_2Fe_{14}B$ anisotropy constants K_1 and K_2 extracted with the Sucksmith-Thompson (ST) method [70]. Although it assumes perfectly aligned Fe and Nd moments, we employ the ST method to have a consistent comparison with experimental anisotropy constants that were also extracted with it. The agreement is fairly good. It is also consistent with Fig. 4: At high temperatures, both anisotropy constants are positive and the phase is therefore uniaxial. At low temperature, the competition between negative K_1 and positive K_2 results in the conical phase. The temperature at which K_1 changes signs is underestimated, consistently with the underestimation of the SRT temperature (Fig. 4).

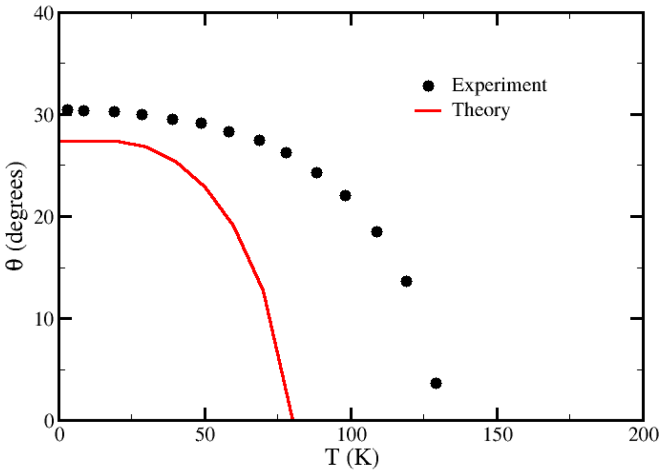

FIG. 4. Temperature evolution of the angle θ between the total moment and the [001] axis (in the (110) plane) in $Nd_2Fe_{14}B$. Experiment is from Ref. [13].

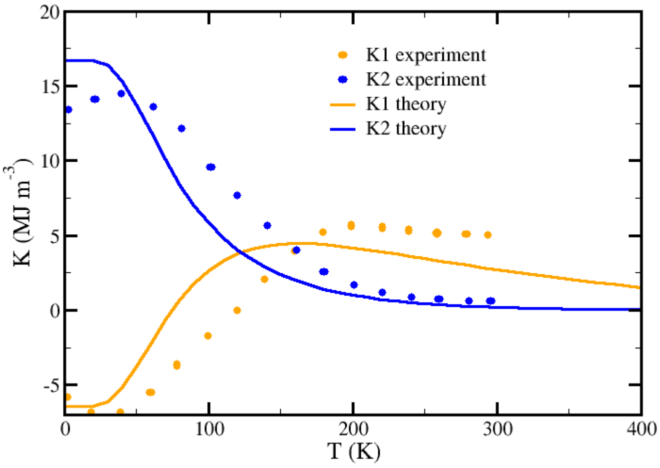

FIG. 5. Evolution of $Nd_2Fe_{14}B$ anistropy constants K_1 and K_2 with temperature, extracted by the Sucksmith-Thompson method [70]. The experimental data was taken from Ref. [58].

Our method therefore proves to be a reliable *ab initio* approach to the magnetic properties of the complicated $Nd_2Fe_{14}B$ system: It provides site-specific Nd CFPs as well as exchange field and explains different subtle experimental features (SRT, FOMP, etc.), with the crystal structure, temperature dependence of the 3*d* magnetic moment and Wannier projection window as the only parameters.

C. Ce substitution

Within the two-sublattice model (cf. Secs. II C–II F), we now turn to partial substitution of Nd by lighter, more abundant, and cheaper Ce whose preferred site is still controversial. Indeed, Ref. [60] showed that Ce favors the smaller *f* site in their compounds (consistently with a valence dominated by Ce^{4+}). However, Ref. [71] suggested the opposite. To investigate this issue, we compared the experimental FOMP at 10 K along [100] in $(Nd_{0.37}Ce_{0.63})_2Fe_{14}B$ with theoretical calculations for different occupancy scenarios (cf. Table II): Ce with a slight *g* preference as measured by Ref. [71] (scenario 1), no site preference between Ce and Nd (scenario 2), Ce with a slight *f* preference as measured by Ref. [60] (scenario 3), and Ce fully occupying the *f* site (scenario 4). As illustrated in Fig. 6, gauged by the FOMP field, scenario 3 gives the best agreement with experiment. However, one may notice that the relative error in the determination of the FOMP field for the pure compound (about 2 Teslas) suggests an accuracy of about 1 Tesla for the mixed case with the error scaled correspondingly to the lower Nd concentration. Within this uncertainty, we cannot discriminate between scenarios 2 and 3; however, Nd preference for the *f* site (scenario 1) and purely *g* Nd occupancy (scenario 4) are unlikely. Therefore, the experimental situation likely corresponds to either no preference or a slight Ce preference for the *f* site. This implies that there is potentially room for site occupancy optimization, which will be studied below.

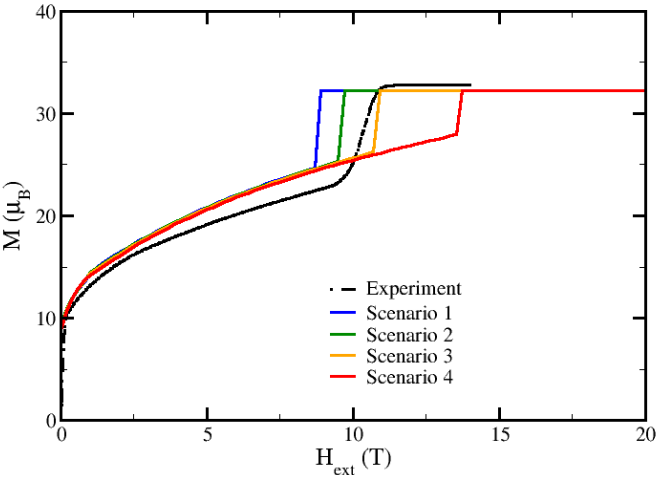

FIG. 6. Magnetization curve of $(Nd_{0.37}Ce_{0.63})_2Fe_{14}B$ (per f.u.) along [100] at 10 K, according to experiment and computed for the different occupancy scenarios 1–4 (cf. Table II).

TABLE II. Site-detailed stoichiometry of $(Nd_{1-x}R_x)_2Fe_{14}B$ compounds (R = Ce, Dy), depending on various occupancy scenarios. Numbers labeling the scenarios are used for clear reference in the main text and figures. No pref. = no site preference between Nd and *R*. *R* on i = ion *R* occupies first the site i. Reference [71] = Ce has a slight preference for the *g* site. Reference [60] = Ce has a slight preference for the *f* site. Reference [72] = Dy has a slight preference for the *f* site. The actual occupation numbers of scenarios 1, 3, 5, and 7 were extracted by interpolation of the measured data displayed in the respective references.

Compound	Scenario	Nd *f*	Nd *g*	*R f*	*R* g
$(Nd_{0.37}Ce_{0.63})_2Fe_{14}B$	1. Ref. [71]	0.45	0.29	0.55	0.71
	2. No pref.	0.37	0.37	0.63	0.63
	3. Ref. [60]	0.25	0.49	0.75	0.51
	4. Ce on *f*	0.0	0.74	1.0	0.26
$(Nd_{0.64}Ce_{0.36})_2Fe_{14}B$	5. Ref. [60]	0.56	0.72	0.44	0.28
	6. Ce on *f*	0.28	1.0	0.72	0.0
$(Nd_{0.64}Dy_{0.36})_2Fe_{14}B$	7. Ref. [72]	0.51	0.77	0.49	0.23
	8. Dy on *g*	1.0	0.28	0.0	0.72

We then computed and measured MAE $= F_{[100]} - F_{[001]}$ for different Ce concentrations: $Nd_2Fe_{14}B$, $(Nd_{0.64}Ce_{0.36})_2Fe_{14}B$, $(Nd_{0.37}Ce_{0.63})_2Fe_{14}B$, and $Ce_2Fe_{14}B$. For the theoretical estimation, we directly evaluated the MAE from Eq. (4) using the experimental occupancy of Ref. [60] for the mixed systems (scenarios 3 and 5 in Table II). The results are displayed in Fig. 7. The MAE decreases, as expected, as a function of the Ce concentration which contributes weakly to the MAE (only through the renormalization of K_1^{3d} in this paper) compared to Nd. The overall agreement between theory and experiment is fairly good, which shows the ability of our approach to treat complex substituted systems.

To investigate the importance of site occupancy, we also computed the MAE with Ce occupying only the *f* site for the $(Nd_{0.64}Ce_{0.36})_2Fe_{14}$ stoichiometry (scenario 6 in Table II); the result is displayed in Fig. 7. Compared to the experimental occupancy of Ref. [60], we computed an increase of anisotropy over the whole range of temperature (+9% at 300 K, for instance, from 2.2 to 2.4 MJ.m^{-3}). This effect arises from the larger Nd *g* SIA due to larger $A_2^0\langle r^2\rangle$ and $B_{\rm ex}$

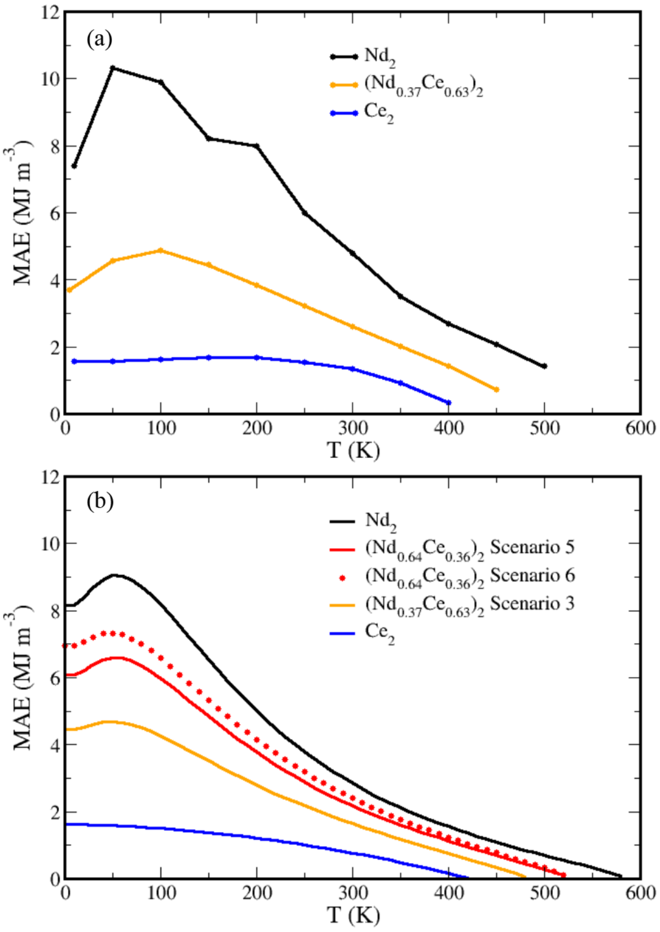

FIG. 7. Magnetocrystalline anisotropy as a function of temperature of $(Nd_{1-x}Ce_x)_2Fe_{14}B$ compounds. (a) Experiment. (b) Theory according to occupancy scenarios of Table II. In the case of $Ce_2Fe_{14}B$, the theoretical MAE amounts to $K_1^{3d}(T)$ as explained in the Methods section.

(as discussed above, cf. Fig. 2). Therefore, by further enhancing f-site Ce occupancy (and, correspondingly, Nd g occupancy) one should be able to increase the MAE of $(Nd, Ce)_2Fe_{14}B$-substituted compounds. It also means that when it comes to nonmagnetic Nd substitutions, it is, in principle, preferable to use elements with smaller ionic radii to keep Nd at the g site.

D. Dy substitution

Within the two-sublattice model (cf. Secs. II C–II E), we now turn to Dy substitution, which is routinely used in the industry to enhance anisotropy in $Nd_2Fe_{14}B$. According to Ref. [72], Dy has a preference for the f site, which is consistent with its smaller atomic radius compared to Nd (lanthanide contraction). As in the case of Ce, the experimental occupancy is still close to equal occupation between sites but the situation is reversed: here, heavy R occupying the f site is expected to be detrimental to the anisotropy. Indeed, as shown in Fig. 8(a), Dy has a larger SIA and also features a larger contribution arising from the g site. It results in $\mathrm{MAE}^g_{\mathrm{Dy}}$-$\mathrm{MAE}^f_{\mathrm{Dy}} > \mathrm{MAE}^g_{\mathrm{Nd}}$-$\mathrm{MAE}^f_{\mathrm{Nd}}$, which means that, for a given Dy content, forcing Dy to occupy the g site is predicted to enhance the anisotropy. This is illustrated in Fig. 8(b): Theoretical MAE of $(Nd_{0.64}Dy_{0.36})_2Fe_{14}B$ with the experimental occupancy from Ref. [72] (scenario 7 in Table II) is larger than in pure $Nd_2Fe_{14}B$ but can be further increased by assuming Dy to occupy the g site (scenario 8 in Table II). We computed, for instance, an increase of 10% at 300 K (from 4.1 to 4.5 MJ.m^{-3}). Therefore, were we able to force Dy on the g site in Nd-Dy compounds, we could increase, though moderately, the anisotropy per Dy content. The same kind of phenomenon is expected to occur with Tb substitution.

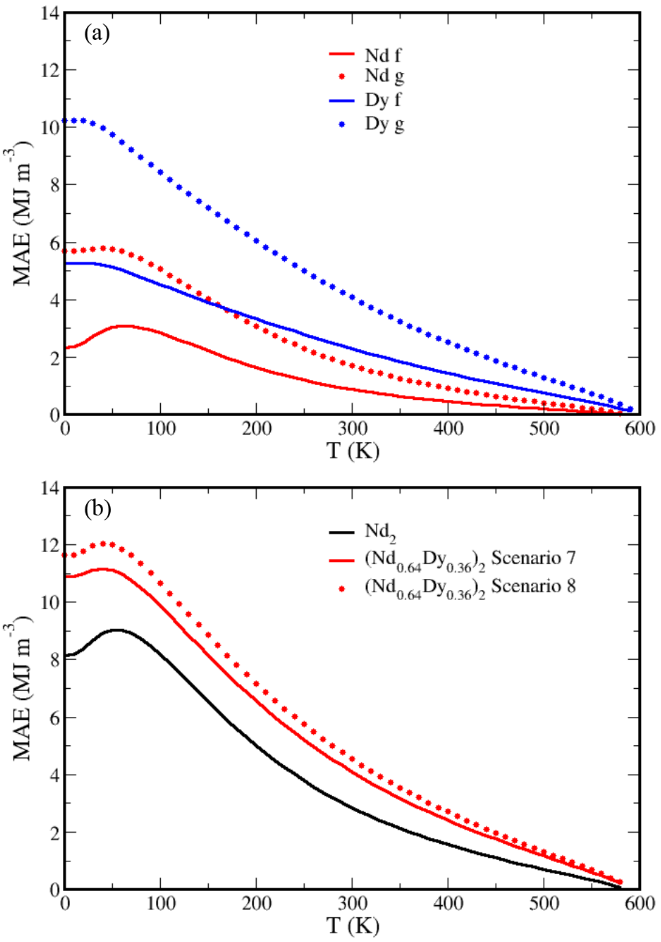

FIG. 8. Evolution of theoretical MAE with temperature. (a) Per (R, site). (b) $Nd_2Fe_{14}B$ and $(Nd_{0.64}Dy_{0.36})_2Fe_{14}B$, according to occupancy scenarios of Table II.

V. CONCLUSION

In this paper, we computed from a first-principles DFT+DMFT approach site-specific crystal-field and exchange-field parameters of Nd in the theoretically challenging $Nd_2Fe_{14}B$ intermetallic, which is the most widely used high-performance hard magnet in the industry. The resulting values are in excellent agreement with previously computed and experimental ones. Moreover, we have shown that these parameters are essentially insensitive to substitutions on the other R site in the 2-14-1 structure, an assumption usually made in the literature but never proven.

TABLE III. Site-specific theoretical CFPs and B_{ex} (in K) for Nd and Dy computed in different compounds. The values are for the R ions in the $z = 0$ plane of the unit cell (the signs of $A_2^{-2}\langle r^2\rangle$, $A_4^{-2}\langle r^4\rangle$, $A_6^{-2}\langle r^6\rangle$, and $A_6^{-6}\langle r^6\rangle$ change for the middle plane). In substituted compounds, Nd/Dy occupies the site indicated in the second column, which is also highlighted by the order of the ions in the compound formula (first ion on site f, second on site g).

	Site	$A_2^0\langle r^2\rangle$	$A_2^{-2}\langle r^2\rangle$	$A_4^0\langle r^4\rangle$	$A_4^{-2}\langle r^4\rangle$	$A_4^4\langle r^4\rangle$	$A_6^0\langle r^6\rangle$	$A_6^{-2}\langle r^6\rangle$	$A_6^4\langle r^6\rangle$	$A_6^{-6}\langle r^6\rangle$	B_{ex}
$Nd_2Fe_{14}B$	f	246	–537	–14	54	–91	–27	–24	–232	78	203
	g	420	349	–41	–29	42	–19	15	–149	–37	222
$NdLaFe_{14}B$	f	297	–641	–22	73	–119	–25	–16	–228	27	212
$CeNdFe_{14}B$	g	414	334	–45	–28	54	–20	9	–154	–56	223
$Dy_2Fe_{14}B$	f	113	–345	–4	29	–19	–12	27	–93	115	209
	g	186	180	–16	–17	19	–10	–14	–25	72	207
$DyCeFe_{14}B$	f	115	–381	–6	32	–21	–14	32	–95	123	189
$CeDyFe_{14}B$	g	190	129	–18	–7	8	–11	–21	–15	86	210

We also show that with these parameters one may construct an almost fully *ab initio* two-sublattice model that reproduces various measured magnetic properties of $Nd_2Fe_{14}B$.

Next, we studied industrially motivated partial substitution of Nd by Ce or Dy, focusing on the substitution site preference and its impact on magnetic properties. In Ce-substituted compounds—often considered in the quest to reduce the scarce heavy rare-earth content in hard magnets—comparison of experimental data [60,71] with our theoretical calculations supports a slight Ce preference for the f site. We carried out experimental measurements of MAE in Ce-substituted single crystals, which are found to be in good agreement with our theoretical predictions. Our calculations also predict that enhancing Nd preferential g-site occupancy leads to a higher SIA. This theoretical observation implies that one might be able to enhance the magnetic anisotropy in $(\mathrm{Nd, Ce})_2\mathrm{Fe}_{14}\mathrm{B}$ compounds by engineering higher Ce f-site occupancy.

In Dy-substituted compounds, routinely used in the industry, we have also shown that an increase—though moderate—of the magnetic anisotropy is theoretically expected when Dy occupies the g site. This could perhaps be achieved by adding a third R element with an even smaller radius (therefore occupying preferably the f site), such as Ce^{4+}: while this kind of doping would lower the anisotropy of the compound, it could increase the anisotropy per Dy atom by the mechanism aforementioned as well as reduce the total economic cost (as Ce is cheaper than Dy), resulting in an overall better anisotropy/price ratio.

Overall, our *ab initio* approach is shown to be a reliable tool to predict and analyze intrinsic properties of complex, substituted, hard magnetic materials. It may provide useful insight into site-occupancy optimization and its impact on magnetic properties.

ACKNOWLEDGMENTS

This work was supported by the future pioneering program Development of Magnetic Material Technology for High-Efficiency Motors (MagHEM) commissioned by the New Energy and Industrial Technology Development Organization (NEDO). A.A. and K.S. acknowledge financial support from the Deutsche Forschungsgemeinschaft–Project-ID No. 405553726-TRR 270. L.P. and J.B. are grateful to the CPHT computer support team.

APPENDIX

Table III summarizes CFPs and exchange fields computed in this paper for various 2-14-1 systems.

---

[1] O. Gutfleisch, M. A. Willard, E. Brück, C. H. Chen, S. G. Sankar, and J. P. Liu, Adv. Mater. **23**, 821 (2011).

[2] J. M. D. Coey, IEEE Trans. Magn. **47**, 4671 (2011).

[3] K. Hono and H. Sepehri-Amin, Scr. Mater. **151**, 6 (2018).

[4] K. Skokov and O. Gutfleisch, Scr. Mater. **154**, 289 (2018).

[5] J. Coey, Engineering **6**, 119 (2020).

[6] M. Kuz'min and A. Tishin, in *Handbook of Magnetic Materials*, edited by K. Buschow (North-Holland, Amsterdam, 2007), Vol. 17, pp. 149–233.

[7] M. D. Kuz'min, Y. Skourski, D. Eckert, M. Richter, K.-H. Müller, K. P. Skokov, and I. S. Tereshina, Phys. Rev. B **70**, 172412 (2004).

[8] C. Fuerst, J. Herbst, and E. Alson, J. Magn. Magn. Mater. **54-57**, 567 (1986).

[9] R. M. Nicklow, N. C. Koon, C. M. Williams, and J. B. Milstein, Phys. Rev. Lett. **36**, 532 (1976).

[10] R. K. Chouhan, A. K. Pathak, D. Paudyal, and V. Pecharsky (2018), arXiv:1806.01990.

[11] X. Liao, L. Zhao, J. Zhang, K. Xu, B. Zhou, H. Yu, X. Zhang, J.-M. Greneche, A. Aubert, K. Skokov *et al.*, J. Mater. Res. Technol. **17**, 1459 (2022).

[12] M. Yamada, H. Kato, H. Yamamoto, and Y. Nakagawa, Phys. Rev. B **38**, 620 (1988).

[13] J. M. Cadogan, J. P. Gavigan, D. Givord, and H. S. Li, J. Phys. F: Met. Phys. **18**, 779 (1988).

[14] N. Kostyuchenko, I. Tereshina, D. Gorbunov, E. Tereshina-Chitrova, K. Rogacki, A. Andreev, M. Doerr, G. Politova, and A. Zvezdin, Intermetallics **124**, 106840 (2020).

[15] M. Ito, M. Yano, N. M. Dempsey, and D. Givord, J. Magn. Magn. Mater. **400**, 379 (2016).

[16] X.-F. Zhong and W. Y. Ching, Phys. Rev. B **39**, 12018 (1989).

[17] X.-F. Zhong and W. Y. Ching, Phys. Rev. B **40**, 5292 (1989).

[18] P. Novák and J. Kuriplach, Phys. Rev. B **50**, 2085 (1994).

[19] K. Hummler and M. Fähnle, Phys. Rev. B **53**, 3272 (1996).

[20] P. Novák, Phys. Status Solidi B **198**, 729 (1996).

[21] M. Diviš, J. Rusz, H. Michor, G. Hilscher, P. Blaha, and K. Schwarz, J. Alloys Compd. **403**, 29 (2005).

[22] C. E. Patrick and J. B. Staunton, Phys. Rev. Materials **3**, 101401(R) (2019).

[23] L. V. Pourovskii, J. Boust, R. Ballou, G. G. Eslava, and D. Givord, Phys. Rev. B **101**, 214433 (2020).

[24] S. Tanaka, H. Moriya, H. Tsuchiura, A. Sakuma, M. Diviš, and P. Novák, J. Phys.: Conf. Ser. **266**, 012045 (2011).

[25] S. Tanaka, H. Moriya, H. Tsuchiura, A. Sakuma, M. Diviš, and P. Novák, J. Appl. Phys. **109**, 07A702 (2011).

[26] T. Yoshioka, H. Tsuchiura, and P. Novák, Mater. Res. Innov. **19**, S4 (2015).

[27] H. Tsuchiura, T. Yoshioka, and P. Novák, Scr. Mater. **154**, 248 (2018).

[28] T. Yoshioka and H. Tsuchiura, Appl. Phys. Lett. **112**, 162405 (2018).

[29] H. Sato, Y. Kubo, T. Yoshioka, H. Tsuchiura, Y. Mizuno, K. Koike, K. Takahashi, and H. Kato, AIP Adv. **11**, 025224 (2021).

[30] P. Delange, S. Biermann, T. Miyake, and L. Pourovskii, Phys. Rev. B **96**, 155132 (2017).

[31] W. Metzner and D. Vollhardt, Phys. Rev. Lett. **62**, 324 (1989).

[32] A. Georges and G. Kotliar, Phys. Rev. B **45**, 6479 (1992).

[33] J. Hubbard, Proc. R. Soc. London A **276**, 238 (1963).

[34] M. Aichhorn, L. Pourovskii, V. Vildosola, M. Ferrero, O. Parcollet, T. Miyake, A. Georges, and S. Biermann, Phys. Rev. B **80**, 085101 (2009).

[35] J. M. Alameda, D. Givord, R. Lemaire, Q. Lu, S. B. Palmer, and F. Tasset, J. Phys. Colloq. **43**, C7-133 (1982).

[36] P. Blaha, K. Schwarz, G. Madsen, D. Kvasnicka, J. Luitz, R. Laskowski, F. Tran, and L. D. Marks, *WIEN2k, An augmented Plane Wave + Local Orbitals Program for Calculating Crystal Properties* (Karlheinz Schwarz, Techn. Universität Wien, Austria, 2018).

[37] J. F. Herbst, Rev. Mod. Phys. **63**, 819 (1991).

[38] D. Givord, H. Li, J. Moreau, R. Perrier de la Bâthie, and E. Du Trémolet de Lacheisserie, Physica B+C **130**, 323 (1985).

[39] P. Blaha, K. Schwarz, F. Tran, R. Laskowski, G. K. H. Madsen, and L. D. Marks, J. Chem. Phys. **152**, 074101 (2020).

[40] O. Parcollet, M. Ferrero, T. Ayral, H. Hafermann, I. Krivenko, L. Messio, and P. Seth, Comput. Phys. Commun. **196**, 398 (2015).

[41] M. Aichhorn, L. Pourovskii, P. Seth, V. Vildosola, M. Zingl, O. E. Peil, X. Deng, J. Mravlje, G. J. Kraberger, C. Martins *et al.*, Comput. Phys. Commun. **204**, 200 (2016).

[42] A. I. Lichtenstein and M. I. Katsnelson, Phys. Rev. B **57**, 6884 (1998).

[43] L. V. Pourovskii, B. Amadon, S. Biermann, and A. Georges, Phys. Rev. B **76**, 235101 (2007).

[44] W. T. Carnall, G. L. Goodman, K. Rajnak, and R. S. Rana, J. Chem. Phys. **90**, 3443 (1989).

[45] J. M. D. Coey, *Rare-Earth Iron Permanent Magnets* (Clarendon Press, Oxford, 1996).

[46] B. Frietsch, J. Bowlan, R. Carley, M. Teichmann, S. Wienholdt, D. Hinzke, U. Nowak, K. Carva, P. M. Oppeneer, and M. Weinelt, Nat. Commun. **6**, 8262 (2015).

[47] M. Pivetta, F. Patthey, I. Di Marco, A. Subramonian, O. Eriksson, S. Rusponi, and H. Brune, Phys. Rev. X **10**, 031054 (2020).

[48] B. G. Wybourne, *Spectroscopic Properties of Rare Earths* (Interscience Publishers, New York, 1965).

[49] K. W. H. Stevens, Proc. Phys. Soc. Sec. A **65**, 209 (1952).

[50] J. Mulak and Z. Gajek, *The Effective Crystal Field Potential* (Elsevier Science, Oxford, 2000).

[51] K. Momma and F. Izumi, J. Appl. Cryst. **44**, 1272 (2011).

[52] C. Liu, Y. X. Yao, C.-Z. Wang, K.-M. Ho, and V. P. Antropov, Phys. Rev. B **102**, 205119 (2020).

[53] F. Bolzoni, J. Gavigan, D. Givord, H. Li, O. Moze, and L. Pareti, J. Magn. Magn. Mater. **66**, 158 (1987).

[54] L. M. García, J. Chaboy, F. Bartolomé, and J. B. Goedkoop, Phys. Rev. Lett. **85**, 429 (2000).

[55] M. D. Kuz'min, Phys. Rev. Lett. **94**, 107204 (2005).

[56] M. D. Kuz'min, D. Givord, and V. Skumryev, J. Appl. Phys. **107**, 113924 (2010).

[57] C. Zener, Phys. Rev. **96**, 1335 (1954).

[58] A. V. Andreev, A. V. Deryagin, N. V. Kudrevatykh, N. V. Mushnikov, V. A. Re'imer, and S. V. Terent'ev, Zh. Éksp. Teor. Fiz. **90**, 1042 (1986) [Sov. Phys. JETP **63**, 608 (1986)].

[59] S. Hirosawa, Y. Matsuura, H. Yamamoto, S. Fujimura, M. Sagawa, and H. Yamauchi, J. Appl. Phys. **59**, 873 (1986).

[60] C. V. Colin, M. Ito, M. Yano, N. M. Dempsey, E. Suard, and D. Givord, Appl. Phys. Lett. **108**, 242415 (2016).

[61] A. Galler, S. Ener, F. Maccari, I. Dirba, K. P. Skokov, O. Gutfleisch, S. Biermann, and L. V. Pourovskii, npj Quantum Mater. **6**, 2 (2021).

[62] G. Gomez Eslava, B. Fayyazi, K. Skokov, Y. Skourski, D. Gorbunov, O. Gutfleisch, N. M. Dempsey, and D. Givord, J. Magn. Magn. Mater. **520**, 167470 (2021).

[63] Y. Skourski, M. D. Kuz'min, K. P. Skokov, A. V. Andreev, and J. Wosnitza, Phys. Rev. B **83**, 214420 (2011).

[64] H. Li, J. Gavigan, J. Cadogan, D. Givord, and J. Coey, J. Magn. Magn. Mater. **72**, L241 (1988).

[65] I. Nowik, K. Muraleedharan, G. Wortmann, B. Perscheid, G. Kaindl, and N. Koon, Solid State Commun. **76**, 967 (1990).

[66] H. Onodera, H. Yamauchi, M. Yamada, H. Yamamoto, M. Sagawa, and S. Hirosawa, J. Magn. Magn. Mater. **68**, 15 (1987).

[67] F. Bartolomé, J. M. Tonnerre, N. Jaouen, D. Raoux, J. Chaboy, L. M. García, H. Maruyama, and R. Steinmann, J. Appl. Phys. **87**, 4762 (2000).

[68] L. M. García, J. Chaboy, F. Bartolomé, and J. B. Goedkoop, J. Appl. Phys. **87**, 6567 (2000).

[69] P. Wolfers, M. Bacmann, and D. Fruchart, J. Alloys Compd. **317-318**, 39 (2001).

[70] W. Sucksmith and J. E. Thompson, Proc. R. Soc. London A **225**, 362 (1954).

[71] Z. Lin, L. Zha, F. Wang, Z. Liu, R. Wu, J. Yang, M. Xue, W. Yang, G. Tian, X. Ma *et al.*, Acta Mater. **200**, 502 (2020).

[72] K. Saito, S. Doi, T. Abe, and K. Ono, J. Alloys Compd. **721**, 476 (2017).